Renewable Energy 250 (2025) 123181

Contents lists available at ScienceDirect

Renewable Energy

journal homepage: www.elsevier.com/locate/renene

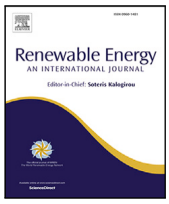

Uncertainty quantification analysis in the blade element momentum method

Guiyu Cao, Zheni Fei, Christopher Vogel *

Department of Engineering Science, University of Oxford, Oxford, UK

ARTICLE INFO

Keywords:
Blade element momentum model
Uncertainty quantification
Uncertainty propagation
Global sensitivity analysis
Offshore wind turbines

ABSTRACT

Blade element momentum (BEM) theory is a widely used non-linear model for the efficient evaluation of wind turbine performance and design. The aim of this paper is to quantify the uncertainty related to BEM inputs and sub-models, and investigate how these propagate through the model. Uncertainties associated with viscous dissipation in the wake, aerofoil force coefficients, and tip-loss models are considered. The uncertainty quantification (UQ) of these parameters is analysed using non-intrusive polynomial chaos expansion, which provides a structured method for uncertainty propagation and global sensitivity quantification. Sobol's indices are employed to rank the relative importance of each factor to the overall uncertainty in the system, with a focus on rotor performance and spanwise load distributions. Two BEM implementations with and without tip-loss correction are used to simulate the NREL 5 MW and DTU 10 MW reference wind turbines. Global sensitivity quantification shows that the different rotors may exhibit different levels of sensitivity to input parameters. The effect of viscous mixing in the turbine wake is found to have a significant impact on predicted rotor performance. Uncertainty in tip-loss model coefficients is also found to be generally important, particularly when evaluating spanwise variations in rotor loads. The Sobol's indices are also observed to depend on the tip speed ratio (TSR), with the most significant uncertainty factors converging for $TSR \geq 6$. We additionally compare global sensitivity analysis to local analysis based on partial derivatives of the uncertainty parameters. The non-linear nature of BEM means that a local analysis does not always capture the interactions between different factors, potentially leading to misleading evaluations of parameter importance. UQ has the potential to improve the understanding of BEM, and provide guidance on the importance of sub-model improvements.

1. Introduction

Blade element momentum (BEM) theory was developed by Glauert [1] for airplane propellers, combining principles of momentum conservation and two-dimensional blade element theory. The methodology has been applied with considerable success to the design and analysis of axial flow rotors, e.g., wind turbines [2] and tidal turbines [3], although many corrections have been developed over time to account for discrepancies between BEM predictions and results from higher fidelity simulations and experiments [4]. Corrections include tip-loss models to account for three-dimensional flow effects near the blade tips [1,2], high-thrust corrections [5,6], and aerofoil data [7]. The non-linear nature of the BEM method means that propagating and quantifying the uncertainties associated with these corrections and their empirical coefficients is non-trivial, impacting upon confidence in engineering models.

This paper presents an uncertainty quantification (UQ) analysis of the non-linear BEM method. UQ analysis has been applied extensively to different non-linear models [8–10]. A key objective of UQ is to evaluate uncertainties in system outputs propagated from uncertain inputs, considering that not all aspects of a system may be known or precisely specified, such as empirical model coefficients or due to *ad hoc* assumptions. UQ analyses can be broadly categorised into two types: intrusive methods [10], in which the governing equations are modified from first principles; and non-intrusive methods [11] which instead estimate and propagate uncertainties via sampling methods. Compared with the extensive modification of the underlying model required to develop stochastic models with intrusive methods [9], a non-intrusive approach is more straightforward to implement, albeit at the cost of needing to iterate the model a sufficient number of times to evaluate UQ metrics.

Non-intrusive polynomial chaos expansion (PCE), based on a spectral representation of the uncertainty, has been investigated extensively as a means of efficient and reliable UQ [11,12]. Non-intrusive PCE can be significantly more computationally efficient than traditional Monte-Carlo-based non-intrusive UQ analysis and allows convenient evaluation of sensitivity indices [13]. In view of its efficiency and reliability, this work adopts PCE-based UQ analysis to evaluate how uncertainty propagates through the BEM.

* Corresponding author.
E-mail addresses: guiyu.cao@eng.ox.ac.uk (G. Cao), zheni.fei@linacre.ox.ac.uk (Z. Fei), christopher.vogel@eng.ox.ac.uk (C. Vogel).

https://doi.org/10.1016/j.renene.2025.123181
Received 26 September 2024; Received in revised form 14 April 2025; Accepted 16 April 2025
Available online 30 April 2025

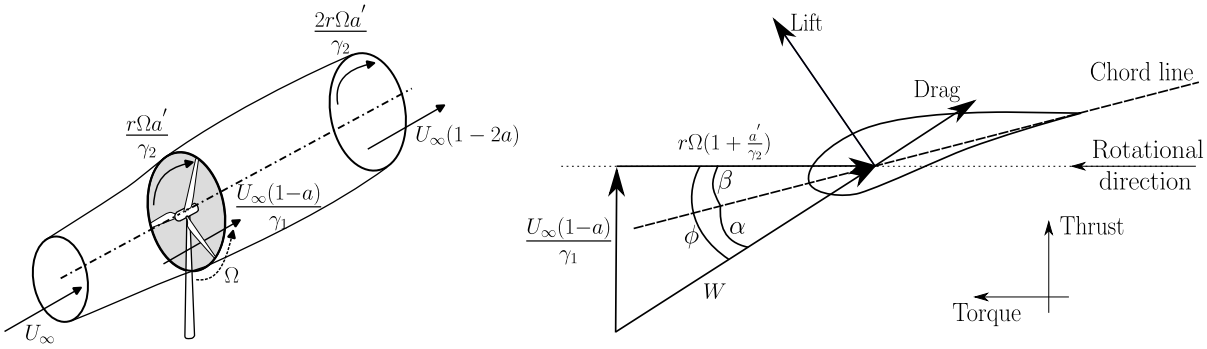

Fig. 1. Illustration of a streamtube passing a wind turbine with important momentum quantities annotated (left), and aerofoil force diagram for blade-element theory (right).

Sensitivity analyses may be local or global. Local analyses evaluate the impact of a small perturbation to model parameters. While relatively simple to evaluate, local analysis can be misleading when the underlying system is non-linear due to the assumed independence between parameters and limited range of perturbation. Global sensitivity analysis (GSA) utilises sampling methods to evaluate uncertainty factors across the feasible space of model parameters, allowing non-linear interactions between inputs to be investigated and the contributions to output variance attributed [14]. Here, we utilise the well-developed variance-based Sobol's method [15] to attribute output variance to each input, building on other applications where PCE-based Sobol's indices have been applied to non-linear models, such as GSA of closure coefficients of turbulence models [12].

To the best of the authors' knowledge, the application of PCE UQ techniques to aerodynamic models for wind turbines, e.g. BEM, actuator disc, or actuator line, is a nascent field [16]. Quantifying the effects of uncertainty and its propagation through the models can help improve confidence in model outputs and aid the understanding and development of empirical corrections. We focus on several areas of uncertainty in the BEM method, associated with induction factors, two-dimensional aerofoil data, and tip-loss modelling, considering different model implementations reported in the literature. The integrated thrust and power coefficients, and the spanwise-varying thrust and power coefficients are considered as output quantities of interest (QoI). Both the NREL 5 MW [17] and DTU 10 MW [18] reference wind turbines at varying tip speed ratio (TSR) are investigated to ensure generality in this study. Partial derivative-based local analysis is also implemented to compare with the GSA.

In the following, BEM uncertainty factors are defined in Section 2. Section 3 briefly introduces non-intrusive polynomial chaos expansion and Sobol's indices. Section 4 presents the cases verification for reference wind turbines. In Section 5, we discuss the UQ analysis results for the reference turbines, and the comparison to local analysis is presented in Section 6. Finally we summarise our findings in Section 7.

2. Uncertainty factors in the blade element momentum model

BEM couples changes in the axial and tangential momentum around a turbine to the forces acting on the blades, see Fig. 1. Here we present adaptations to BEM to incorporate uncertainty parameters associated with the derivation of induction factors, the utilisation of tabulated lift and drag coefficients, and the *ad hoc* modelling of empirical tip-loss correction function; for a thorough review of BEM theory the reader is referred to texts such as [6].

2.1. Momentum equations

The principle of conservation of momentum is applied to consider the balance between the pressure drop across the rotor and the far-field change in the momentum flux under the assumption of inviscid flow. Viscous dissipation in the wake has the effect of introducing uncertainty in the inviscid calculation of pressure drop across the rotor. Considering viscous effects in the wake region, Bernoulli's theorem is applied separately upstream and downstream of the rotor, which gives

$$\frac{1}{2}\rho(U_\infty^2 - U_w^2) \equiv \gamma_1 \Delta p, \tag{1}$$

where ρ is fluid density, and U_∞ and U_w are the velocities far upstream and far downstream of the rotor respectively. We define an uncertainty factor γ_1, and the static pressure drop across the rotor is Δp, where the static pressure is equal to atmospheric. Physical arguments require the uncertainty factor $\gamma_1 \geq 1$, where unity corresponds to inviscid flow.

An expression for the flow speed through the rotor plane U_d can be found by equating Δp acting over the rotor face with the thrust considering the change in axial momentum of the flow

$$U_d = \frac{1}{2}\frac{1}{\gamma_1}\left(U_\infty + U_w\right) = \frac{1}{\gamma_1}(1-a)U_\infty \tag{2}$$

where we define $U_w \equiv (1-2a)U_\infty$ in terms of an axial induction factor a for mathematical convenience (see Fig. 1). Consequently, applying conservation of axial momentum to an annular section of the rotor, the annular thrust coefficient C_t reads

$$C_t = \frac{\mathrm{d}T}{\frac{1}{2}\rho U_\infty^2 2\pi r dr} = \frac{1}{\gamma_1}4a(1-a), \tag{3}$$

where $\mathrm{d}T$ is the annular thrust force and r the local radius.

Analogous to the axial momentum, uncertainty in the tangential momentum balance is considered by introducing the parameter γ_2 associated with the tangential induction factor a', as shown in Fig. 1. The tangential induction factor a' is defined in the tangential velocity at the rotor plane $(U_t)_d$ such that $(U_t)_d \equiv (1+a')\Omega r$, where Ω is the angular velocity of rotor. The overall change in tangential velocity reads

$$\Delta U_t = (U_t)_w - (U_t)_\infty = 2a'\Omega r, \tag{4}$$

where $(U_t)_d$ is assumed to reach half its downstream value $(U_t)_w$ in the wake region, with the assumption of the incoming tangential velocity $(U_t)_\infty = 0$. Considering the unsteady inflows (e.g., swirling turbulent inflow or coherent gusts) to impose a perturbation on $(U_t)_\infty$, we introduce the uncertainty in the change of tangential velocity across the rotor plane as

$$\Delta U_t = (U_t)_w - (U_t)_\infty \equiv \frac{1}{\gamma_2}2a'\Omega r, \tag{5}$$

where uncertainty factor γ_2 is associated with the tangential induction factor a'. Through conservation of angular momentum, the annular torque coefficient C_m normalising the annular torque $\mathrm{d}M$ is modified to

$$C_m = \frac{\mathrm{d}M}{\frac{1}{2}\rho U_\infty^2 r 2\pi r dr} = \frac{1}{\gamma_1\gamma_2}4a'(1-a)\lambda_r, \tag{6}$$

where $\lambda_r = \Omega r/U_\infty$ is the local speed ratio.

A tip correction k_m is applied to account for differences between the actuator disc and a turbine with a finite blades, modifying the thrust coefficient and the torque coefficient to become

$$C_t = \frac{1}{\gamma_1} 4a(1-a)k_m, \quad C_m = \frac{1}{\gamma_1\gamma_2} 4a'(1-a)k_m\lambda_r. \tag{7}$$

The subscript m is used to denote that the correction is applied to the momentum equations. Following [1], the tip-loss correction factor k_m reads

$$k_m = \frac{2}{\pi}\cos^{-1}\left\{\exp\left[-\frac{B(R-r)}{2r\sin\phi}\right]\right\}, \tag{8}$$

where B is the number of blades, R the radius of blades, and the flow angle ϕ is the angle between the local relative velocity W and the rotor plane as shown in Fig. 1.

2.2. Blade element theory

Two-dimensional aerofoil theory, illustrated in Fig. 1, also provides expressions for C_t and C_m by considering the aerodynamic forces acting on a blade section. In Fig. 1, the flow angle ϕ and the relative velocity W read

$$\tan\phi = \frac{\gamma_2}{\gamma_1}\left(\frac{1-a}{\gamma_2+a'}\right)\frac{1}{\lambda_r}, \quad W = \frac{(1-a)U_\infty}{\gamma_1\sin\phi}. \tag{9}$$

With the predefined blade twist angle β, the angle of attack α can be obtained as $\alpha = \phi - \beta$. The thrust force and torque on a complete annular segment at radius r and encompassing B blades of chord length c reads

$$\mathrm{d}T = \frac{1}{2}\rho W^2(Bc\mathrm{d}r)c_x, \quad \mathrm{d}M = r\frac{1}{2}\rho W^2(Bc\mathrm{d}r)c_y, \tag{10}$$

where the coefficients $c_x = c_l\cos\phi + c_d\sin\phi$ and $c_y = c_l\sin\phi - c_d\cos\phi$, with the sectional lift and drag coefficients c_l and c_d, respectively, functions of the angle of attack α. From blade element theory, we thus obtain the annular thrust and torque coefficients as

$$C_t = \frac{1}{\gamma_1^2}\left(\frac{1-a}{\sin\phi}\right)^2\sigma_s c_x, \quad C_m = \frac{1}{\gamma_1^2}\left(\frac{1-a}{\sin\phi}\right)^2\sigma_s c_y, \tag{11}$$

where the solidity ratio is defined $\sigma_s = Bc/2\pi r$.

In blade element theory, the assumption of radial independence does not reflect the observed reduction in loads towards the blade tip. This can lead to over-prediction of rotor thrust and torque, and thus correction methods have been proposed to rectify the lack of pressure equalisation [19]. We denote such blade-based corrections with k_b (e.g. [2]), distinct from those such as the Glauert correction [1] which account for the lack of discrete blades in the disc representation. Consequently, the thrust and torque coefficients are modified to become

$$C_t = \frac{1}{\gamma_1^2}\left(\frac{1-a}{\sin\phi}\right)^2\sigma_s c_x k_b, \quad C_m = \frac{1}{\gamma_1^2}\left(\frac{1-a}{\sin\phi}\right)^2\sigma_s c_y k_b, \tag{12}$$

with

$$k_b = \frac{2}{\pi}\cos^{-1}\left\{\exp\left[-g\frac{B(R-r)}{2r\sin\phi}\right]\right\}. \tag{13}$$

The empirical function g reads

$$g = \exp\left[-c_1(B\lambda - c_2)\right] + 0.1, \tag{14}$$

where the calibrated values $c_1 = 0.125$, and $c_2 = 21$ are adopted [2], $\lambda = \Omega R/U_\infty$ is the tip-speed ratio. Inherent *adhoc* uncertainty in the factors c_1 and c_2 results from the empirical calibration process, since there does not yet exist a universal form of g for wind turbines. We therefore investigate the effect of uncertainty in c_1 and c_2 on the overall rotor performance QoIs.

Table 1
Implementations of BEM: S_0 - no tip loss corrections; S_1 - only momentum correction; S_2 - momentum and blade-element corrections.

Scheme	Momentum equation	Blade-element equation
S_0	Eqs. (3) & (6)	Eq. (11)
S_1	Eq. (7)	Eq. (11)
S_2	Eq. (7)	Eq. (12)

2.3. Aerofoil data

In practical cases, the lift and drag forces realised along the rotor blade may diverge from the tabulated values for two-dimensional aerofoils for various reasons, including the effects of turbulent inflows, Reynolds number variations, blade surface roughness, etc. Thus, uncertainties in the practical lift coefficient c_l and drag coefficient c_d are introduced as

$$c_l = (1+\eta_1)c_l^*, \quad c_d = (1+\eta_2)c_d^*, \tag{15}$$

where c_l^* and c_d^* are the tabulated clean aerofoil data. In Eq. (15), η_1 and η_2 are sampled from a modelling distribution to quantify the uncertainties for c_l and c_d; here we adopt Gaussian distributions as

$$\eta_i(\alpha) \equiv \frac{1}{\delta_i\sqrt{2\pi}}\exp\left[-\frac{(\alpha-\alpha_b)^2}{2\delta_i^2}\right], \tag{16}$$

where α_b is the local angle of attack when solving the BEM equations but neglecting the influence of uncertainty parameters for the same operating conditions. In Eq. (16), both α_b and α are normalised by the unit degree to guarantee that the perturbation η_i is dimensionless. δ_i is the standard deviation of η_i, $i = 1, 2$, describing the uncertainty in c_l and c_d, respectively. Fig. 2 shows an illustration to the perturbation of lift coefficient.

2.4. BEM method implementations

Applying conservation of mass and moment fluxes around the rotor, equating the expressions for C_t and C_m derived from the momentum and blade-element equations yields non-linear expressions for induction factors a and a' which are solved iteratively within the BEM [20,21].

In the current work, three implementations of nonlinear BEM listed in Table 1 are investigated. There are no tip-loss corrections in Scheme S_0. For scheme S_1, the tip-loss correction as in Eq. (8) is applied to the momentum equations only. For scheme S_2, the tip-loss corrections as in Eqs. (8) and (13) are applied to both the momentum equations and blade-element equations, respectively.

For scheme S_0, the update of a and a' is given by

$$a = \frac{\sigma_s c_x}{\sigma_s c_x + 4\gamma_1\sin^2\phi}, \quad a' = \frac{\gamma_2}{\gamma_1}\frac{\sigma_s c_y(1-a)}{4\lambda_r\sin^2\phi}. \tag{17}$$

For scheme S_1, the combination of Eqs. (7) and (11) leads to

$$a = \frac{\sigma_s c_x}{\sigma_s c_x + 4\gamma_1 k_m\sin^2\phi}, \quad a' = \frac{\gamma_2}{\gamma_1}\frac{\sigma_s c_y(1-a)}{4k_m\lambda_r\sin^2\phi}. \tag{18}$$

For scheme S_2, the combination of Eqs. (7) and (12) leads to

$$a = \frac{\sigma_s c_x k_b}{\sigma_s c_x k_b + 4\gamma_1 k_m\sin^2\phi}, \quad a' = \frac{\gamma_2}{\gamma_1}\frac{\sigma_s c_y k_b(1-a)}{4k_m\lambda_r\sin^2\phi}. \tag{19}$$

Additionally, at high axial induction factor, momentum theory breaks down and the so-called high thrust Glauert correction [2] is applied to S_0 as

$$C_t = \frac{1}{\gamma_1}4\left[a_c^2 + (1-2a_c)a\right], \quad a > a_c. \tag{20}$$

Similarly, the correction for S_1 and S_2 reads

$$C_t = \frac{1}{\gamma_1}4\left[a_c^2 + (1-2a_c)a\right]k_m, \quad a > a_c. \tag{21}$$

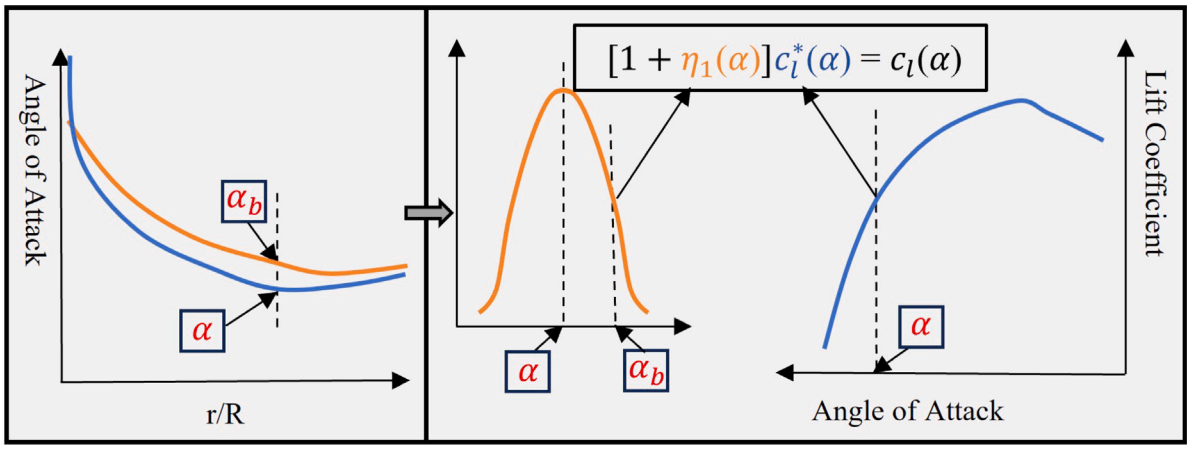

Fig. 2. Illustration of the perturbation of lift coefficient, where α_b is pre-determined from a BEM solution neglecting influence of uncertainty factors. α and c_l are updated in each iteration of the BEM implementation.

The critical axial induction value is set as $a_c = 1/3$.

We initialise a and a' to be zero, and iteratively calculate the flow angle ϕ with Eq. (9) and thus the angle of attack α to update the estimates for the sectional force coefficients c_x and c_y and thereby a and a'. In all schemes S_0, S_1, and S_2, the convergence criterion are evaluated at step n as $\left\|a^n - a^{n-1}\right\| / \left\|a^{n-1}\right\| \le \varepsilon$ and $\left\|a'^n - a'^{n-1}\right\| / \left\|a'^{n-1}\right\| \le \varepsilon$ where $\|\|$ represents the absolute value. We employ $\varepsilon = 10^{-3}$ in this work to guarantee converged solutions. Once a and a' are established, QoIs such as distributed thrust coefficient C_t and power coefficient C_p can be calculated, where $C_p = C_m \times \lambda_r$. The integrated thrust coefficient C_T and power coefficient C_P can be obtained by the numerical integration along the rotor, such as the analytical formula $C_T = \frac{1}{A}\int_0^R C_t 2\pi r dr$ with $A = \pi R^2$.

3. Non-intrusive polynomial chaos expansion and Sobol's indices

In this section, the non-intrusive polynomial chaos expansion [11,12] and Sobol's decomposition [13,15] are briefly introduced. PCE is widely employed for efficient uncertainty propagation, providing the mean and variance of model outputs based on the approximate response surface created by orthogonal polynomials. PCE-based Sobol's indices are applied in efficiently ranking the relative contributions of each uncertainty factor to the overall variation of the QoI.

In PCE, a d-dimensional set of stochastic input variables are defined as $\boldsymbol{\xi} = \{\xi_1, \xi_2, \ldots, \xi_d\}$. Here, $\boldsymbol{\xi}$ refers to the stochastic inputs of the uncertainty factors introduced in Section 2, namely, the random inputs of γ_1, γ_2, δ_1, δ_2, c_1 and c_2. The output quantities of interest (e.g., the thrust and power coefficients) $Y(\boldsymbol{x}, \boldsymbol{\xi})$ are expressed as functions of $\boldsymbol{\xi}$ and the solution space $\boldsymbol{x}$ (e.g., the radial location). The approximate response surface [11] is represented with the truncated series of orthogonal multivariate polynomials as

$$Y(\boldsymbol{x}, \boldsymbol{\xi}) \approx \Sigma_{i=0}^{N_s} \omega_i(\boldsymbol{x}) \boldsymbol{\Psi}_i(\boldsymbol{\xi}), \tag{22}$$

with the deterministic response coefficient $\omega_i(\boldsymbol{x})$ and pre-determined multivariate polynomials $\boldsymbol{\Psi}_i(\boldsymbol{\xi})$ for ith mode. In Eq. (22), the total number of samples N_s is evaluated as

$$N_s = n_p \left[\frac{(p+d)!}{p!d!}\right], \tag{23}$$

where n_p is the oversampling ratio used to achieve a good approximation [12] and p is the order of polynomial chaos. A detailed explanation of $\boldsymbol{\Psi}_i(\boldsymbol{\xi})$ and the order of polynomial chaos p can be found in Appendix 2 of [13]. The choice of orthogonal multivariate polynomials is determined by the distribution of stochastic input variable ξ_i [9], such as the uniform distribution and Gaussian distribution requiring the Legendre polynomials and Hermite polynomials, respectively. The response coefficient $\omega_i(\boldsymbol{x})$ can be determined based on the orthogonality and integral properties of orthogonal multivariate polynomials [11,22]. After determining $\omega_i(\boldsymbol{x})$, the mean $\mu(\boldsymbol{x})$ and the variance $\sigma^2(\boldsymbol{x})$ of the QoI are computed directly

$$\mu(\boldsymbol{x}) = \omega_0(\boldsymbol{x}), \quad \sigma^2(\boldsymbol{x}) = \Sigma_{i=1}^{N_s} \omega_i^2(\boldsymbol{x}) E[\boldsymbol{\Psi}_i^2(\boldsymbol{\xi})], \tag{24}$$

which is employed for uncertainty propagation, where $E[\cdot]$ represents the expectation in d-dimensional space.

Variance-based Sobol's indices can be efficiently obtained with the PCE response coefficients [12,13]. The total variance $D(\boldsymbol{x}) \equiv \sigma^2(\boldsymbol{x})$ can be decomposed as

$$D(\boldsymbol{x}) = \Sigma_{i=1}^{d} D_i(\boldsymbol{x}) + \Sigma_{1\le i<j\le d}^{d-1} D_{i,j}(\boldsymbol{x}) + \Sigma_{1\le i<j<k\le d}^{d-2} D_{i,j,k}(\boldsymbol{x}) + \cdots + D_{1,2,\ldots,d}(\boldsymbol{x}). \tag{25}$$

The partial variances $D_{i_1,\ldots,i_s}$ are given by

$$D_{i_1,\ldots,i_s}(\boldsymbol{x}) = \Sigma_{\boldsymbol{\epsilon}\in\Gamma_{i_1,\ldots,i_s}} \omega_{\boldsymbol{\epsilon}}^2(\boldsymbol{x}) E[\boldsymbol{\Psi}_{\boldsymbol{\epsilon}}^2(\boldsymbol{\xi})], \quad 1 \le i_1 < \cdots < i_s \le d, \tag{26}$$

where detailed definitions of the integer sequence $\boldsymbol{\epsilon}$, the set $\Gamma_{i_1,\ldots,i_s}$ for $\boldsymbol{\epsilon}$ tuples, and the multivariate polynomial $\boldsymbol{\Psi}_{\boldsymbol{\epsilon}}$ can be found in [13]. $E[\cdot]$ represents the expectation in s-dimensional space. The Sobol's indices $S_{i_1,\ldots,i_s}(\boldsymbol{x})$ are defined as the partial variances relative to the total variance

$$S_{i_1,\ldots,i_s}(\boldsymbol{x}) = \frac{D_{i_1,\ldots,i_s}(\boldsymbol{x})}{D(\boldsymbol{x})}. \tag{27}$$

The first-order Sobol's indices $S_i(\boldsymbol{x})$ provide a sensitivity measure of the individual contribution from each input uncertainty factor ξ_i. The total-order Sobol's indices $S_{T_i}(\boldsymbol{x})$ is defined as the summation of all partial Sobol's indices related to ξ_i. $S_{T_i}(\boldsymbol{x})$ is given by

$$S_{T_i}(\boldsymbol{x}) = \Sigma_{L_i} S_{i_1,\ldots,i_s}(\boldsymbol{x}), \tag{28}$$

where $L_i = \{(i_1, \ldots, i_s) : \exists k, 1 \le k \le s, i_k = i\}$. In comparison to the first-order index $S_i(\boldsymbol{x})$, total-order index $S_{T_i}(\boldsymbol{x})$ represents contributions from all possible interaction effects among ξ_i and the other input uncertainty factors. Sobol's indices can be used to rank the relative contribution of each input uncertainty to the overall output variability, including consideration of the non-linear correlation between input uncertainty factors and output QoI [12]. The larger the Sobol's index, the relatively greater the importance of that uncertainty factor to the QoI.

4. Cases verification for reference turbines

This section presents the verification of our in-house BEM code with a comparison to QBlade [23] predictions for two reference wind turbines across a range of TSR. QBlade is a user-friendly and open

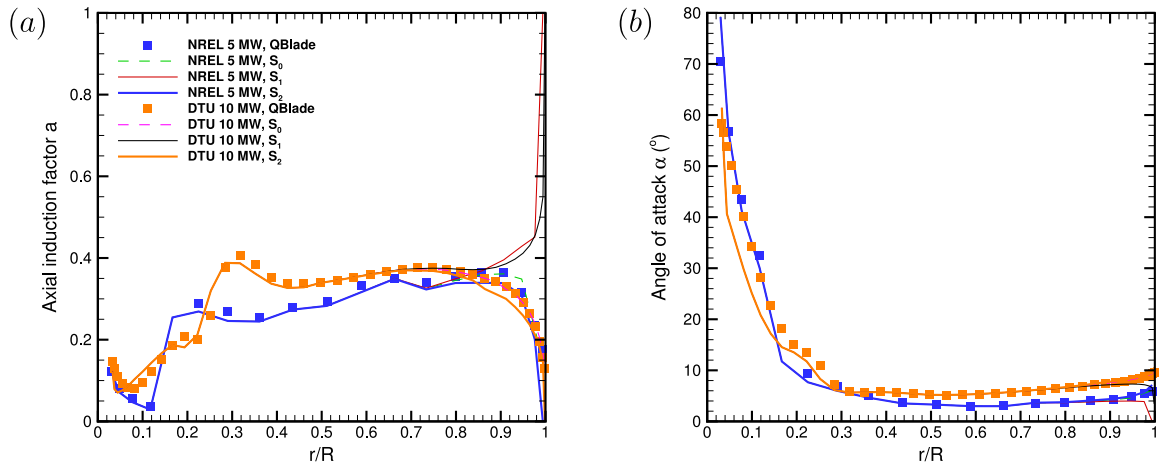

Fig. 3. Spanwise distributions of axial induction factors a (left) and angle of attack α (right) at TSR = 8 for the NREL 5 MW and DTU 10 MW reference turbines. Comparison is made to QBlade results and three BEM implementation schemes.

source code for the simulation of wind turbines and aerodynamic design of rotor blades that has been extensively validated for steady BEM analysis [24]. We have made comparisons to QBlade as a widely-used software in the wind energy community for our bespoke BEM implementation that allows us to also consider how the uncertainty parameters affect BEM predictions of turbine performance.

The NREL 5 MW reference turbine [17] and the DTU 10 MW reference turbine [18] are simulated with three schemes S_0, S_1 and S_2. To minimise potential sources of error between our in-house code and QBlade, we use the same aerofoil lift and drag data relevant to the reference turbines in both codes. For analysis of the BEM, the rotors were discretised into 19 and 40 evaluation points for the NREL 5 MW and DTU 10 MW reference turbines, respectively.

Fig. 3 shows the spanwise distributions of axial induction factor a and angle of attack α at TSR = 8 for both reference turbines as predicted by QBlade and our BEM solutions with different sub-models. In terms of axial induction factor a, the S_0 scheme solution agrees well with that from QBlade. Under scheme S_1, a rapidly approaches 1 near the tip region, which is also observed in [2]. We observe only small difference in the distribution of a between S_2 and S_0 schemes. In terms of angle of attack α, solutions from the current three schemes agree well with the reference solution for the NREL 5 MW reference turbine, except for a sharper drop in the near-tip region with S_1 scheme. For the DTU 10 MW reference turbine, the difference between the current simulations and the reference solution is mainly observed in the $0.05 \leq r/R \leq 0.30$ inboard region. These differences may arise from the different treatments in the iterative solution process, e.g., the specific BEM model and the applied corrections.

Fig. 4 shows the integrated power coefficient C_P and integrated thrust coefficient C_T as functions of the varying TSR. Compared with the integrated power coefficient C_P from QBlade, the S_0 scheme predicts a slightly higher value, whereas both S_1 and S_2 schemes provide slightly lower solutions. $\|C_P(S_i) - C_P(QBlade)\| / \|C_P(QBlade)\|$ (the relative difference) is within 5% across the simulated TSR range, where S_i; $i = 1, 2, 3$ represents the BEM scheme solutions. For the integrated thrust coefficient C_T, we find the magnitude of the solutions are ranked $S_0 > S_1 > S_2$. In general, the S_1 solutions (Prandtl-Glauert correction only) are found to follow the QBlade solutions for both C_P and C_T most closely. In summary, compared with the solutions from QBlade, the current BEM implementations perform well and provide converged solutions for the subsequent UQ analysis. Current verification provides the baseline α_b for following UQ analysis.

5. Uncertainty quantification analysis

We first outline the settings used for the UQ analysis, followed by demonstration of the insights that can be generated using uncertainty quantification analysis applied to the NREL 5 MW and DTU 10 MW reference wind turbines, at different tip-speed ratios, with the S_1 and S_2 schemes.

Table 2
Assumed parameter intervals for uniformly distributed uncertainty factors.

Uncertainty factor	γ_1	γ_2	δ_1	δ_2	c_1	c_2
Interval	[1.0, 1.1]	[0.9, 1.1]	[1.0, 10.0]	[1.0, 10.0]	[0.09, 0.17]	[13, 22]

5.1. UQ analysis parameters

As presented in Section 2, we introduce six uncertainty factors, namely, γ_1, γ_2, δ_1, δ_2, c_1 and c_2. Without *a priori* knowledge of uncertainty factor distributions, they are assumed to be uniformly distributed in this paper.

We consider physical arguments to inform the closed interval for each uncertainty factor, presented in Table 2. Viscous dissipation means that γ_1 should be not less than 1, whereas we allow γ_2 to vary around 1. Following Eq. (16), the intervals of δ_1 and δ_2 impose a maximum perturbation up to 25% of baseline α_b. The baseline α_b of each run is found from solving the BEM equations for the same rotor and operating conditions but neglecting the influence of the uncertainty factors. In terms of α_b for S_2, the default calibrated parameters $c_1 = 0.125$ and $c_2 = 21$ are used. The closed intervals of c_1 and c_2 are chosen to bound the scattered model parameters [19] which were calibrated from blade-resolved simulations.

For the S_1 scheme without tip-loss correction, the combination of factors $(\gamma_1, \gamma_2, \delta_1, \delta_2)$ is used, while all six factors are used for the S_2 scheme with tip-loss correction. Latin hypercube sampling (LHS) [25] is used to generate sampling points from the combination of uncertainty factors, as this method ensures that each input factor has all portions of its distribution represented in the uncertainty assessment.

The accuracy and convergence of the PCE coefficients as functions of n_p and p in Eq. (23) are evaluated by GSA of each uncertainty factor using the total-order Sobol's indices for the rotor power C_P and thrust C_T coefficients. In the following analysis, the total number of samples N_s is determined with $n_p = 2$ and $p = 4$. Additionally, using $d = 4$ and $d = 6$ for the S_1 scheme and S_2 scheme, yields a total of 140 and 420 samples respectively.

The UQ analysis is conducted using openTURNS [26], a widely-used data analysis and modelling tool. In openTURNS, adaptive sparse PCE based on least angle regression [22] is used to determine the expansion coefficients in Eq. (22), which is more efficient than least squares regression in determining deterministic response coefficient

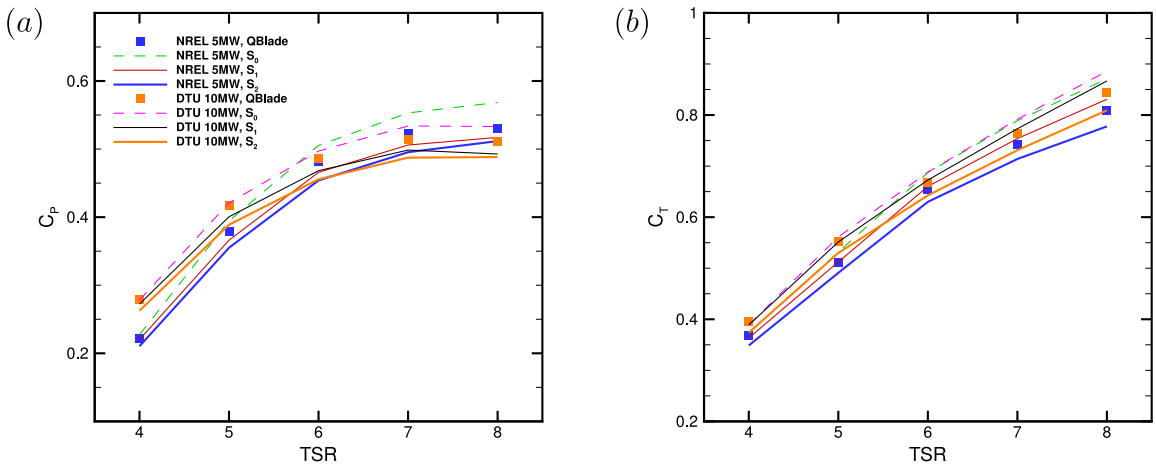

Fig. 4. Comparison of QBlade and in-house BEM solutions for integrated power coefficient C_P (left) and integrated thrust coefficient C_T (right) as functions of TSR for the NREL 5 MW and DTU 10 MW reference turbines.

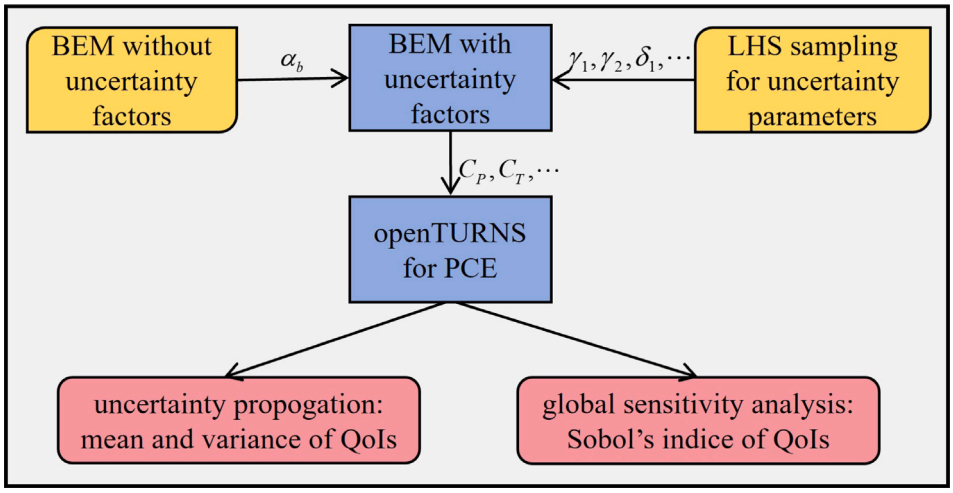

Fig. 5. Flowchart for implementing uncertainty quantification in the BEM, using Latin hypercube sampling of uncertainty parameters and polynomial chaos expansion to evaluate the variance in BEM quantities of interest.

$\omega_i(\mathbf{x})$ without loss of accuracy. For our setup, we find the relative error is smaller than 10^{-4} [22], which ensures convergence of the Sobol's indices.

In the following, PCE is employed for uncertainty propagation, predicting the mean and variance of output QoI. PCE-based Sobol's indices are applied in ranking the relative sensitivity of each uncertainty factor. A flowchart to illustrate the uncertainty quantification of BEM is shown in Fig. 5.

5.2. UQ analysis at TSR = 8

First, we discuss the uncertainty propagation for the integrated QoIs, followed by the global sensitivity analysis and local analysis.

5.2.1. Uncertainty propagation

Fig. 6 shows the rotor power C_P and thrust C_T coefficients for the NREL 5 MW and DTU 10 MW reference turbines, operating at TSR = 8 with the scatter reflecting the effects of uncertainty. Broad agreement of mean (μ) and standard deviation (σ) is observed between the C_P values evaluated using schemes S_1 and S_2, whereas there is a greater difference between C_T computed with the two schemes. $\mu(C_T)$ is somewhat larger for the S_1 scheme than that from the S_2 scheme. Quantitatively, for the NREL 5 MW reference turbine, $\sigma(C_T)$ is 0.0225 and 0.0333 with S_1 and S_2 schemes, respectively. For the DTU 10 MW reference turbine, $\sigma(C_T)$ is 0.0307 and 0.0375 with S_1 and S_2 schemes, respectively. The $\sigma(C_T)$ is higher under the S_2 scheme for both rotors, indicating sensitivity to the tip-loss model, described further below.

Fig. 7 shows the spanwise variation in the contribution to power and thrust coefficients along the blade. Both rotors are evaluated at TSR = 8, and the standard deviations are calculated from the range of solutions across different uncertainty factor values. For both rotors, the variation in mean μ and standard deviation σ of the power coefficient C_p is almost identical for both schemes S_1 and S_2 along much of the rotor blade, although a slightly faster reduction is observed in the tip region $r/R > 0.9$. Greater differences are observed in C_t predictions between the S_1 and S_2 schemes from a radial station $r/R > 0.6$, with the addition of the Shen tip-loss model driving the thrust coefficient down in the S_2 scheme. Additionally, greater variability is observed around the mean $\mu(C_t)$ value in the tip region in the S_2 predictions than the S_1 predictions, indicating sensitivity to the tip-loss model parameters.

5.2.2. Global sensitivity analysis

Fig. 8 shows the first-order and total-order Sobol's indices for power C_P and thrust C_T coefficients for the reference turbines at TSR = 8. The first-order Sobol's indices quantify the effect of each uncertainty factor on QoI individually, while the total-order Sobol's indices quantify the total effect of the ith factor including interactions with other factors. The small difference only observed in c_1 and c_2 between the first-order and total-order Sobol's indices indicates very weak interactions

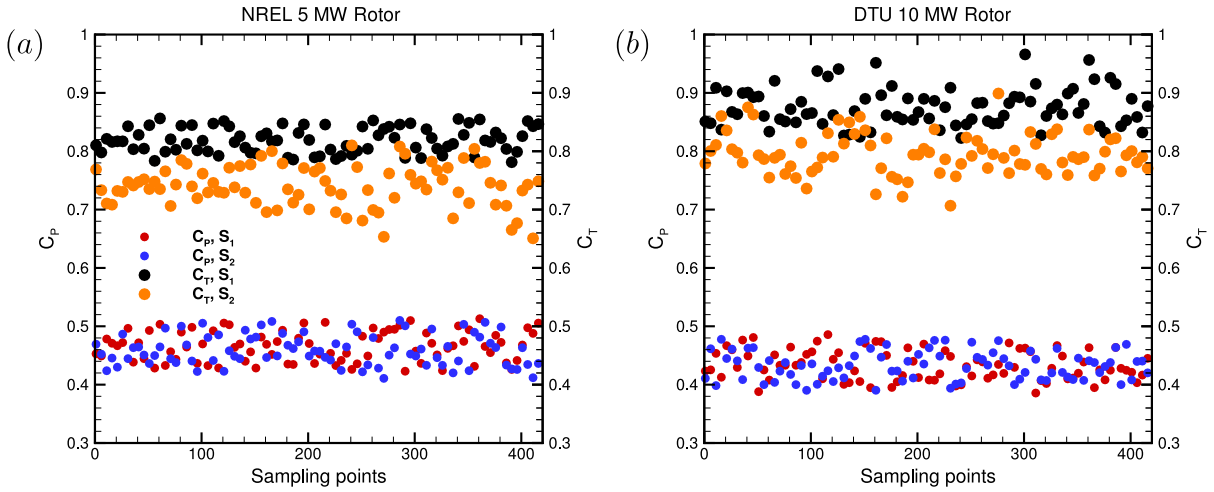

Fig. 6. Evaluations of the integrated power C_P and thrust C_T coefficients with schemes S_1 and S_2 for the NREL 5 MW and DTU 10 MW reference turbines operating at TSR = 8. Scatter is due to the different uncertainty parameter values.

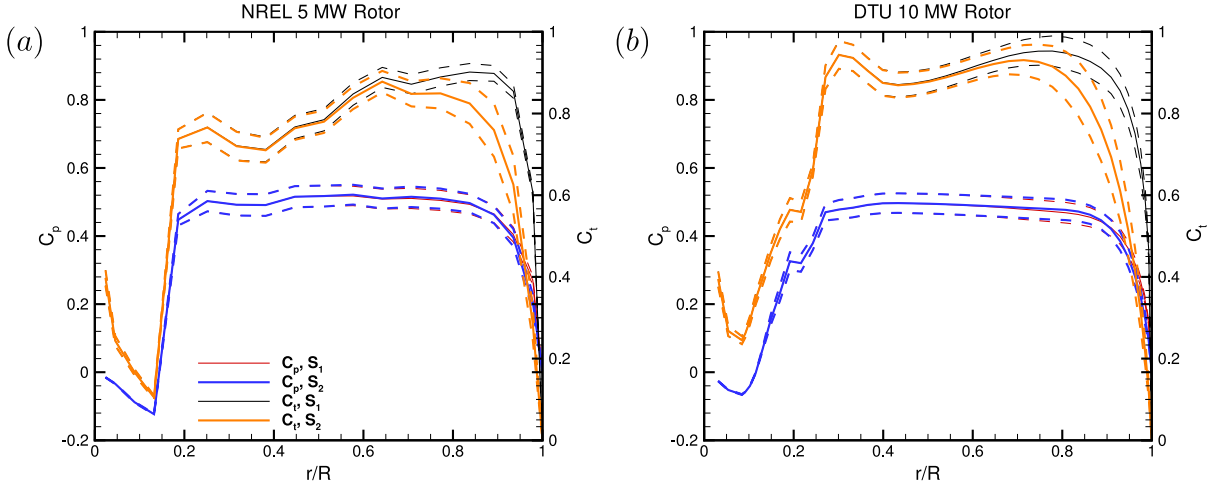

Fig. 7. Spanwise variation in the mean and standard deviation of power C_p and thrust C_t coefficients with NREL 5 MW and DTU 10 MW reference turbines at TSR = 8. Solid lines are the spanwise mean values (μ), and the dashed lines represent the spanwise mean ± standard deviations ($\mu \pm \sigma$).

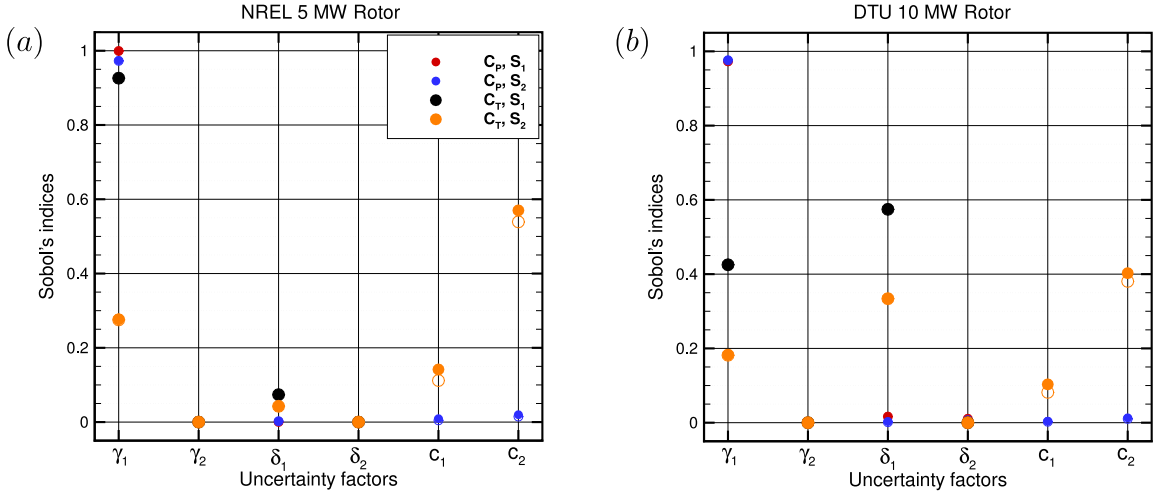

Fig. 8. Total-order (solid circles) and first-order (open circles) Sobol's indices for integrated power C_P and thrust C_T coefficients with NREL 5 MW and DTU 10 MW reference turbines at TSR = 8.

among the uncertainty factors. The first-order and total-order Sobol's indices are almost identical for γ_1, γ_2, δ_1 and δ_2, indicating very little interaction amongst uncertainty factors for the rotor metrics. In the following analysis, we focus on the total-order Sobol's indices.

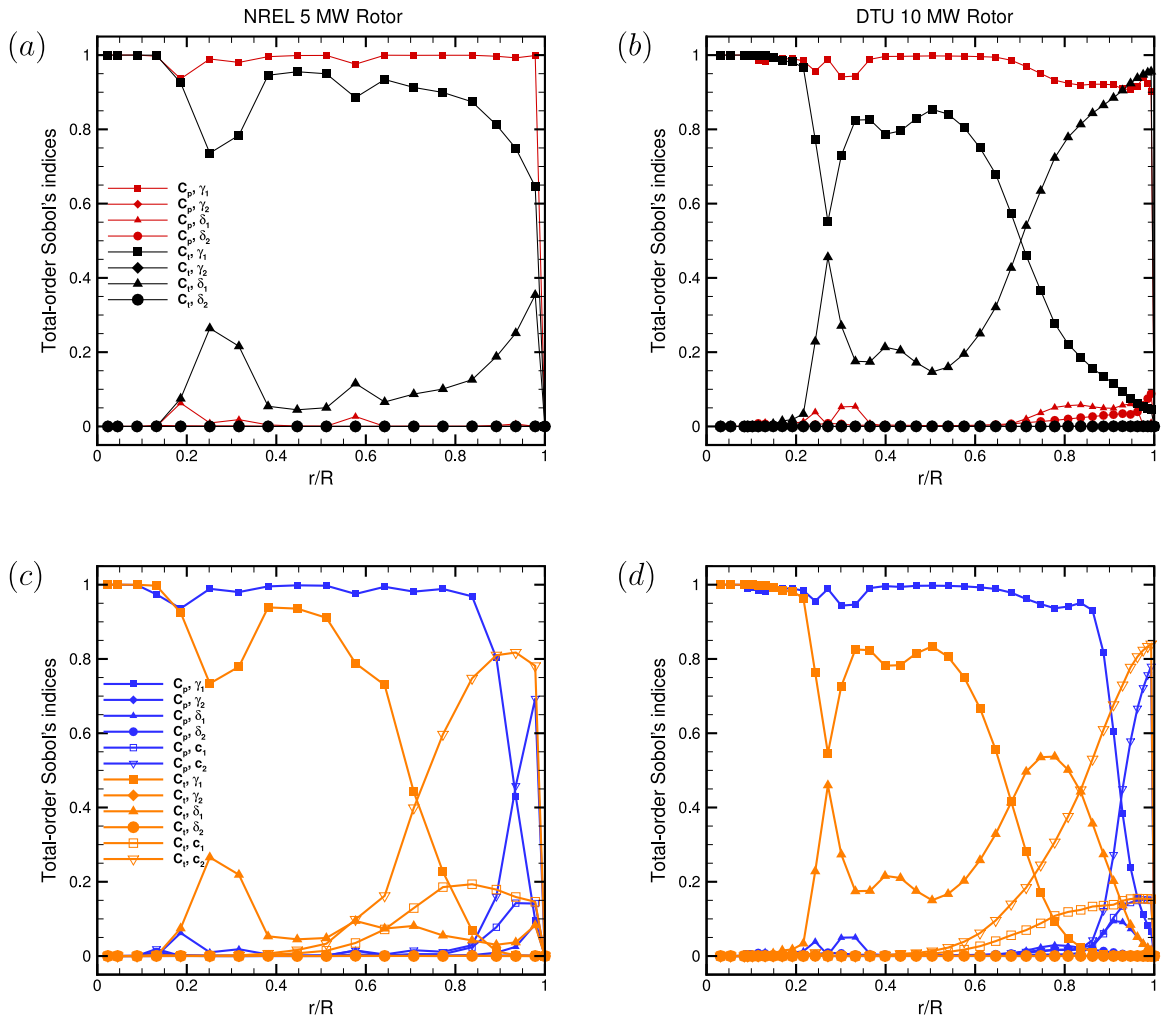

Fig. 9. Spanwise variations in total-order Sobol's indices for the power coefficient C_p and the thrust coefficient C_t with NREL 5 MW (left column) and DTU 10 MW (right column) reference turbines at TSR = 8. Scheme S_1 (a)(b), scheme S_2 (c)(d).

In Fig. 8, we observe that γ_1, associated with viscous mixing in the wake, is the dominant parameter affecting the power coefficient C_P in both schemes S_1 and S_2. The sensitivity of C_T is more complicated: γ_1 is most important with a small contribution from δ_1, associated with the lift coefficient, identified for the NREL 5 MW rotor in scheme S_1; whereas in S_2, introducing the Shen tip-loss model results in γ_1 and the tip-loss parameters c_1 and c_2 being identified as significant factors, again with a small contribution from δ_1. The relative importance of these factors is somewhat different for the DTU 10 MW rotor: at TSR = 8, the pressure term γ_1 is identified as dominating C_P in both schemes, whereas for C_T the lift coefficient factor δ_1 is relatively more important in both schemes than it was for the NREL 5 MW rotor. γ_1 and the tip-loss factors c_1 and c_2 (in scheme S_2) remain important for C_T. Table 3 provides summaries of significant Sobol's indices ≥ 0.1 for the rotors at TSR = 8. For both rotors, C_P is dominated by γ_1, while the relative significance of factors for C_T depends on the tip-loss scheme and the rotor.

Fig. 9 presents the spanwise total-order Sobol's indices for the spanwise power and thrust coefficients. For the distributed power coefficient C_p, γ_1 is the dominant uncertainty factor in the S_1 and S_2 schemes for both rotors, indicating the relative importance of pressure drop across the rotor in predicting the spanwise power. As the tip-loss correction comes to play in the near-tip region, the relative importance of tip-loss parameter c_2 outweighs that of γ_1 in the near-tip region ($r/R \geq 0.9$) for the S_2 scheme. For the distributed thrust coefficient C_t, γ_1 and δ_1 are significant in the S_1 scheme for both rotors, with the lift coefficient factor δ_1 becoming most important in the $r/R \geq 0.7$ region for the DTU 10 MW reference turbine. As expected, the tip-loss factors c_1 and c_2 are shown to be relatively more important near the blade tip in the S_2 scheme, leading to decreases in the relative importance of γ_1 and δ_1 in the near-tip regions for both rotors. Parameter c_2 is always found to be more important than c_1.

Table 3
Significant uncertainty factors for NREL 5 MW and DTU 10 MW reference turbines at TSR = 8 as a function of solution scheme.

Rotors	NREL 5 MW		DTU 10 MW	
Scheme	S_1	S_2	S_1	S_2
C_P	γ_1	γ_1	γ_1	γ_1
C_T	γ_1	c_2, γ_1, δ_1	δ_1, γ_1	c_2, δ_1, γ_1

In summary, the relative importance of the uncertainty factors varies along the rotor blade, and are observed to vary at different rates for the two rotors when operating at the same tip-speed ratio. The implementation of the BEM method also matters: when a tip-loss model is included to account for assumptions about radial independence, the parameters for this model significantly affect near-tip load predictions.

5.3. Global sensitivity analysis with varying TSR

This section focuses on UQ analysis for the reference rotors, varying TSR. Fig. 10 shows total-order Sobol's indices of the integrated power

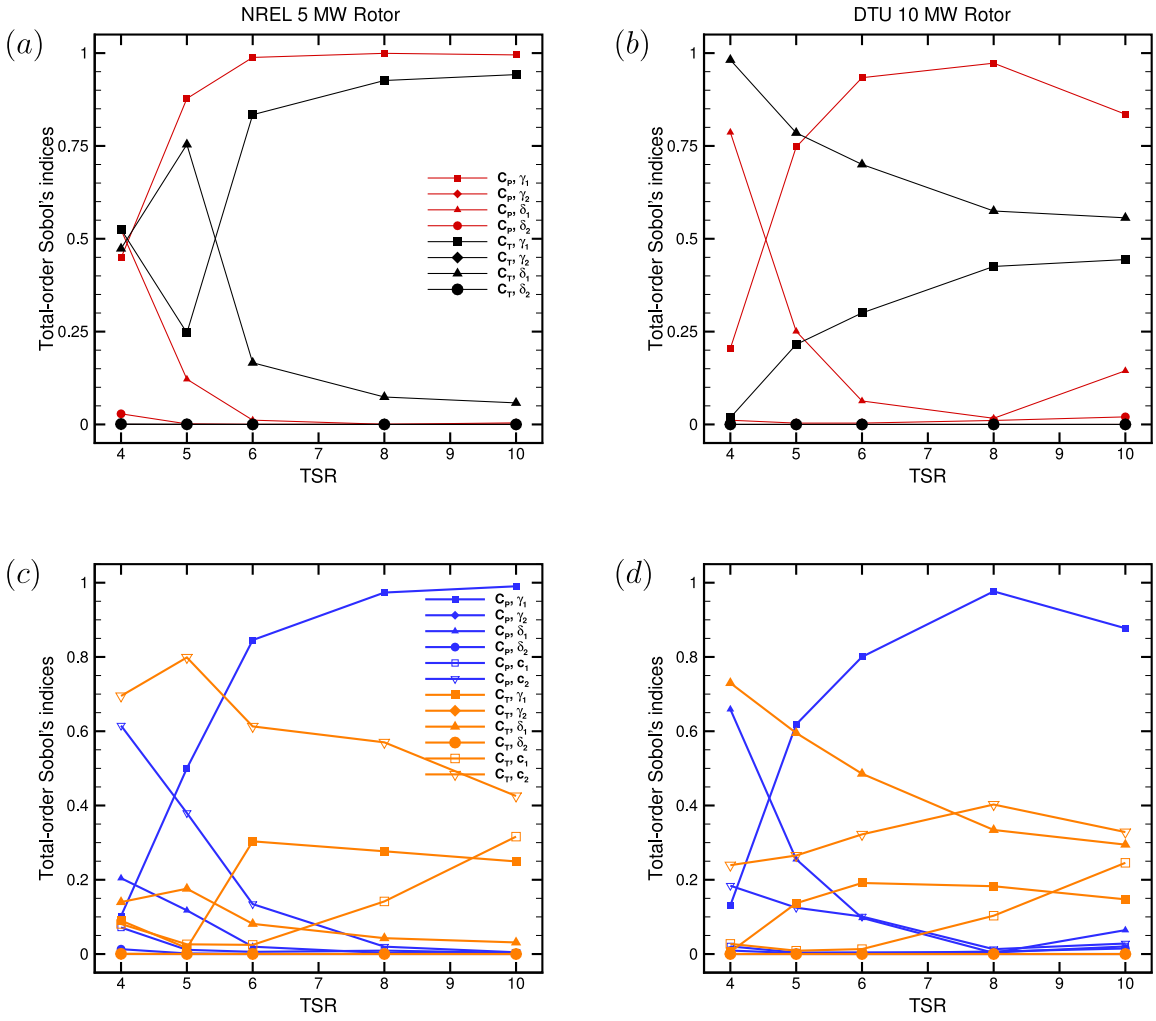

Fig. 10. Total-order Sobol's indices for the integrated power coefficient C_P and the integrated thrust coefficient C_T as functions of TSR for the NREL 5 MW (left column) and DTU 10 MW (right column) reference turbines. Scheme S_1 (a)(b), scheme S_2 (c)(d).

coefficient C_P and the integrated thrust coefficient C_T varying TSR between 4 and 10. We observe differing relative importance amongst the uncertainty factors both for S_1 scheme and S_2 scheme, becoming more stable at higher TSR (≥6). The mean significant uncertainty factors at TSR = 6, 8 and 10 are presented in Table 4. Sobol's indices from two rotors contribute equally at each TSR, i.e., $S^w_{T_i} = (S^n_{T_i} + S^d_{T_i})/2$, where $S^w_{T_i}$, $S^n_{T_i}$, $S^d_{T_i}$ are the mean Sobol's indices, and Sobol's indices for the NREL 5 MW and DTU 10 MW rotors, respectively. As before, the threshold for $S^w_{T_i}$ is set as 0.1 when defining the significant uncertainty factors.

For the S_1 scheme with no tip-loss model, γ_1 is the dominant uncertainty factor for the integrated power coefficient C_P, whereas γ_1 and δ_1 are the most significant uncertainty factors for C_T. For the S_2 scheme, the tip-loss correction in the blade-element part introduces two additional significant uncertainty parameters. It is observed that c_1 becomes more important at high TSR. The uncertainties in c_1 and c_2 may reduce the robustness of S_2 scheme, since universal values of c_1 and c_2 have not yet been determined.

We focus on the UQ analysis of distributed C_t considering the particularly significant uncertainty factors γ_1, δ_1 and c_2. Fig. 11 shows the total-order Sobol's indices for two rotors at TSR = 6, 8, and 10, which qualitatively show the same trends across TSR for the three most significant uncertainty factors. For the S_1 scheme, the relative importance of γ_1 and δ_1 is comparable in the $0.2 \le r/R \le 0.4$ and $0.7 \le r/R \le 1.0$ regions. In terms of the S_2 scheme, we observe the gradually increasing importance of the Shen tip-loss parameter c_2 in the near-tip $0.6 \le r/R \le 1.0$ region, with corresponding decreases in the importance of γ_1 and δ_1. At $r/R = 0.2 - 0.3$ and with increasing TSR, both the stall location and the trough of Sobol's indices for γ_1 moves inboard, but the peak location of Sobol's indices are not always consistent with the stall location. With increasing TSR, the relative importance of c_2 decreases as the relative importance of c_1 increases. Similar observations can be made for the distributed C_p (the detailed result is omitted here).

Table 4
Mean significant uncertainty factors based on $S^w_{T_i}$ with TSR = 6, 8 and 10.

TSR	6		8		10	
Scheme	S_1	S_2	S_1	S_2	S_1	S_2
C_P	γ_1	γ_1, c_2	γ_1	γ_1	γ_1	γ_1
C_T	γ_1, δ_1	c_2, δ_1, γ_1	γ_1, δ_1	c_2, γ_1, δ_1, c_1	γ_1, δ_1	c_2, c_1, γ_1, δ_1

6. Comparison to local analysis

Local analysis based on the evaluation of partial derivatives of uncertainty parameters can be relatively simple to perform. However, such analyses may miss non-linear interactions between uncertainty parameters. A comparison between global sensitivity analysis and local analysis is made to highlight the importance of the GSA framework for analysing non-linear models of turbine performance.

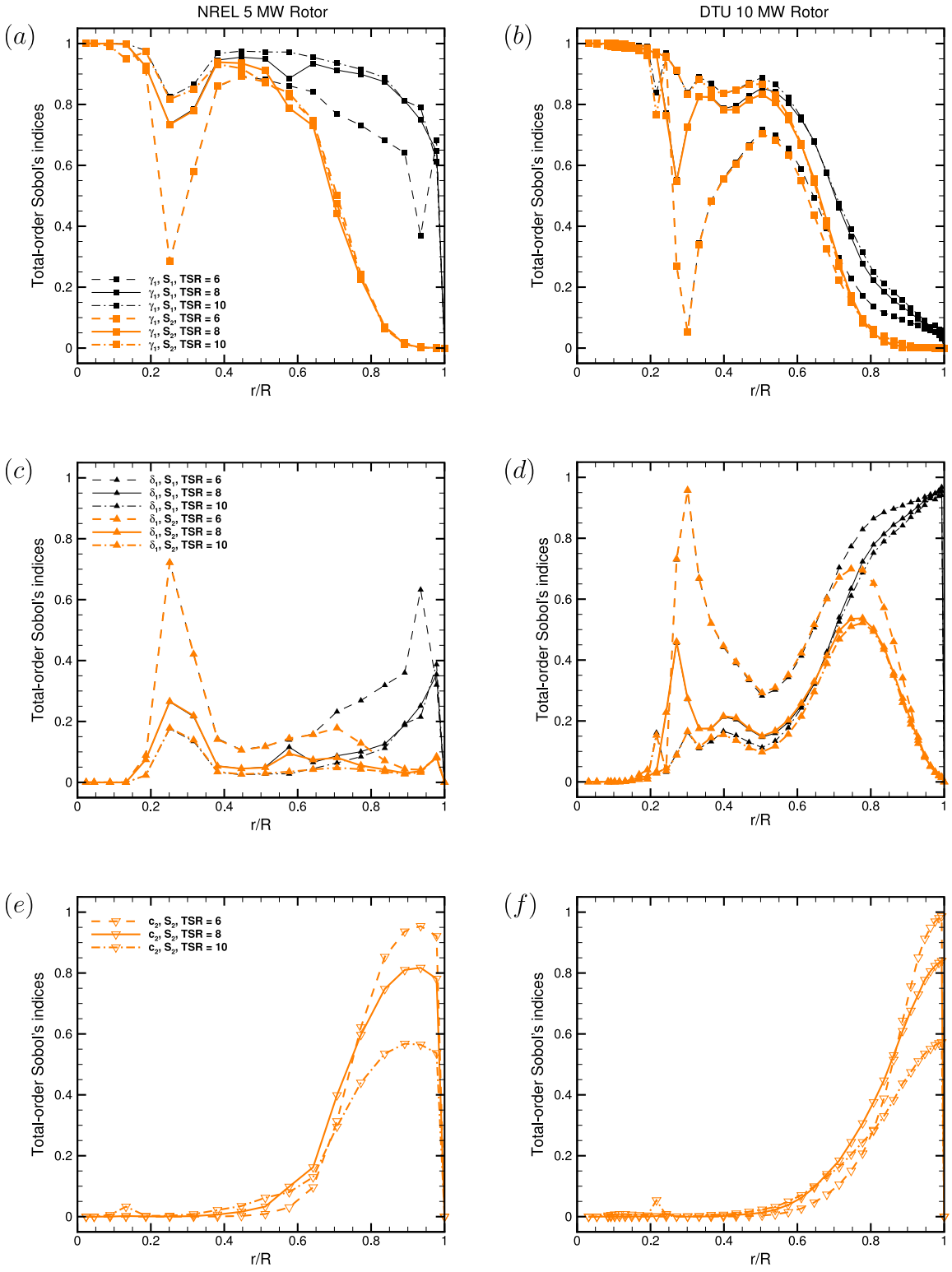

Fig. 11. Total-order Sobol's indices of the spanwise thrust coefficient C_t for the NREL 5 MW (left column) and DTU 10 MW (right column) reference turbines at TSR = 6, 8 and 10. γ_1 (a)(b), δ_1 (c)(d), c_2 (e)(f).

6.1. Partial derivative analysis

The global sensitivity analysis demonstrated that uncertainty parameters γ_1, δ_1 and c_2 are relatively more important in the pairs (γ_1, γ_2), (δ_1, δ_2), and (c_1, c_2), respectively. An alternative local analysis is presented below to understand the relatively more important uncertainty factor in each pair. In Eq. (9), the uncertainties of γ_1 and γ_2 affect the flow angle ϕ. The ratio of partial derivatives is given by

$$\left\| \frac{\partial(\tan\phi)/\partial\gamma_1}{\partial(\tan\phi)/\partial\gamma_2} \right\| = \frac{\gamma_2(\gamma_2 + a')}{\gamma_1 a'} > 4, \tag{29}$$

where it is found that $\|a'\|$ is less than 0.15 for both rotors. Thus, the effect of uncertainty caused by γ_1 in the flow angle is relatively more important than that of γ_2.

Table 5
First-order derivative of c_l^* and total-order C_t Sobol's indices of δ_1 for the DTU 10 MW reference turbine at TSR = 6.

Location	$r/R = 0.7$	$r/R = 0.8$	$r/R = 0.9$
Airfoil	FFA-W3-301	FFA-W3-241	FFA-W3-241
α_m	8.79	9.22	9.48
$(\mathrm{d}c_l^*/\mathrm{d}\alpha)\|_{\alpha_m}$	0.0998	0.104	0.102
Total-order Sobol's indices of S_1	0.663	0.856	0.913
Total-order Sobol's indices of S_2	0.642	0.663	0.279

Table 6
First-order derivative of c_l^* and total-order C_t Sobol's indices of δ_1 for the DTU 10 MW reference turbine at TSR = 8.

Location	$r/R = 0.7$	$r/R = 0.8$	$r/R = 0.9$
α_m	5.21	5.93	6.62
$(\mathrm{d}c_l^*/\mathrm{d}\alpha)\|_{\alpha_m}$	0.120	0.115	0.113
Total-order Sobol's indices of S_1	0.493	0.765	0.877
Total-order Sobol's indices of S_2	0.462	0.510	0.231

For c_1 and c_2, we calculate the ratio of partial derivatives as

$$\left\| \frac{\partial g/\partial c_1}{\partial g/\partial c_2} \right\| = \left\| \frac{B\lambda - c_2}{c_1} \right\| \geq 11.76, \tag{30}$$

with $B = 3$, $\lambda = 8$, and the predefined intervals of c_1 and c_2. With Eq. (30), local analysis shows that the effect of uncertainty in the tip-loss parameter g caused by c_1 is more important than that of c_2.

For induction factor uncertainty parameters, (γ_1, γ_2), the local analysis is consistent with the GSA. Meanwhile, for the tip-loss parameter pair (c_1, c_2), the local analysis contradicts the GSA. In view of the different QoIs in local analysis and GSA, i.e., ϕ and g for local analysis in comparison to rotor thrust C_T and power C_P for GSA, the difference in assessment metrics can lead to differences in the evaluated significance of parameters if the non-linear BEM model is not used to propagate the uncertainties.

6.2. Aerofoil data analysis

For δ_1 and δ_2, it is straightforward to analyse the separate contributions of lift and drag coefficients to $c_x = c_l \cos\phi + c_d \sin\phi$, and $c_y = c_l \sin\phi - c_d \cos\phi$. In c_x and c_y, considering the typically large lift drag ratio c_l/c_d characteristic of airfoils, we have

$$c_l \cos\phi \gg c_d \sin\phi, \quad c_l \sin\phi > c_d \cos\phi, \tag{31}$$

where $c_l \sin\phi > c_d \cos\phi$ is obtained *posteriori* in the $r/R > 0.16$ region for both rotors. This indicates that perturbations of c_l affect c_x and c_y more significantly than that of c_d. For the pair (δ_1, δ_2), the local analysis is consistent with the GSA.

To better understand the role of the lift coefficient uncertainty parameter δ_1, we perform a local analysis for the DTU 10 MW rotor at TSR = 6 and TSR = 8. Uncertainties in lift coefficient could, for example, arise from surface roughness or erosion of rotor blades [27]. In Fig. 11, GSA with both S_1 and S_2 schemes shows the growth of relatively greater importance of δ_1 outboard of $r/R = 0.6$ across all TSRs. We focus on the first-order derivative of the clean lift coefficient $\mathrm{d}c_l^*/\mathrm{d}\alpha$ in the outboard region of the blade. Larger $\mathrm{d}c_l^*/\mathrm{d}\alpha$ will lead to larger discrepancy in lift coefficient when evaluating the uncertainty of α as given in Eq. (16).

Three outboard points at $r/R = 0.7, 0.8, 0.9$ are monitored to investigate the relation between the local gradient $\mathrm{d}c_l/\mathrm{d}\alpha$ and the total-order Sobol's indice for the spanwise thrust coefficient C_t. The first-order Sobol's indices of δ_1 are almost identical to the total-order Sobol's indices, indicating very weak interactions between the uncertainty parameters for the quantities of interest, hence we do not present them separately here. We first determine the mean angle of attack α_m for these monitored points as shown in Fig. 12(a). For the relevant aerofoils, we can also obtain $\mathrm{d}c_l^*/\mathrm{d}\alpha$ as shown in Fig. 12(b). Tables 5 and 6 show weak correlation between the local gradient $(\mathrm{d}c_l^*/\mathrm{d}\alpha)|_{\alpha_m}$ and the global total-order Sobol's index for the thrust coefficient C_t both for S_1 and S_2 schemes. Although δ_1 shows relatively greater importance in these two regions through GSA, it does not appear to be strongly correlated with a large first-order derivative of the clean lift coefficient. Similar to the analysis from Eq. (30), for the nonlinear BEM, this comparison confirms again the inconsistency in interpretation of sensitivity that can arise between local analysis and GSA.

In summary, this highlights the importance of the non-linear BEM in propagating uncertainty impacts through the system and the potential for reaching misleading conclusion if only considering a local analysis of uncertainty parameters.

7. Conclusion

Blade element momentum (BEM) theory is a widely-used nonlinear model of turbine performance. However, it relies on a number of assumptions and sub-models which introduce uncertainties into its predictions and restrict confidence when performing loading evaluations and design of wind turbines. To shed light on the uncertainty in the non-linear BEM, this paper presents a framework for uncertainty quantification (UQ) analysis including uncertainty propagation and global sensitivity analysis (GSA) for the NREL 5 MW and DTU 10 MW reference wind turbines. For the first time, six uncertainty factors relating to assumptions around the momentum equations, tabulated lift and drag coefficients, and the empirical tip-loss correction function are proposed. Non-intrusive polynomial chaos expansion (PCE) is used to propagate these uncertainties through the non-linear BEM model, allowing their importance to be ranked with Sobol's indices and allowing the mean and variance of turbine performance metrics to be assessed.

For uncertainty propagation, applying a tip-loss correction to account for three dimensional blade flows not only increases model complexity, but also reduces the robustness of the BEM implementation. This was reflected in the importance of the tip-loss parameters in scheme S_2, particularly near the blade tip, where accurately specifying parameter c_2 of the Shen tip-loss model is found to be particularly important. PCE-based Sobol's indices are applied in ranking the relative importance of each uncertainty factor. Regardless of model implementation, the effect of viscous mixing on the static pressure drop, summarised in γ_1, was found to be the most significant source of uncertainty in predicting rotor performance coefficients. Sensitivity to input parameters was observed to vary slightly between the two rotors, with the DTU rotor more sensitive to the tabulated lift data than the NREL 5 MW turbine when predicting the thrust coefficient.

The Sobol's indices were observed to depend on the tip speed ratio (TSR). While the relative importance of the uncertainty parameters varied at low TSR, the most significant parameters remained unchanged for TSR $\geq$ 6 for the integrated power coefficient and the integrated thrust coefficient. This is positive for the robust evaluation of the aerodynamic performance near the operating TSR of wind turbines.

Local analysis based on partial derivatives was also implemented to determine locally significant uncertainty factors. However, we found that inconsistent conclusions between the local analysis and the GSA in the nonlinear BEM could be drawn for uncertainty parameters related to tip loss models. Non-linear interactions between parameters may be overlooked when considering only the partial derivatives as demonstrated in the case of the tip-loss parameters. Whilst a similar conclusion on the relative importance of uncertainty in aerofoil lift compared to drag was reached using local and global analyses, the lift coefficient gradient was not particularly strongly correlated with the global variance calculated for PCE-based Sobol's indices.

UQ analysis has the potential to improve understanding of uncertainties in non-linear turbine models, such as the BEM method, and identify particular aspects of the modelling that require careful

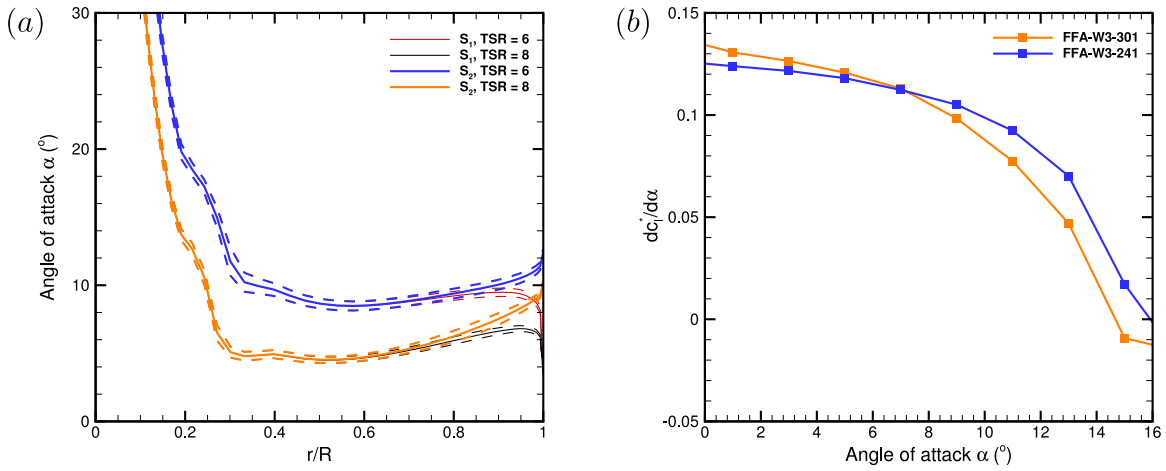

Fig. 12. The spanwise μ (solid lines) and $\mu \pm \sigma$ (dashed lines) of angle of attack α at TSR = 6 and 8, and the first-order derivative of the clean lift coefficients for outboard aerofoils for the DTU 10 MW reference turbine.

attention or sub-model refinement. When proposing modified versions of BEM, the balance between accuracy, complexity and robustness should be considered. The framework presented in this paper can be applied to other rotors, and modified to account for different uncertainty parameters and disturbances. This work will be extended to investigate further sensitivities of turbine models to tip-loss corrections and aerofoil force coefficients, particularly considering effects such as aerodynamic roughness.

CRediT authorship contribution statement

Guiyu Cao: Writing – review & editing, Writing – original draft, Visualization, Software, Methodology, Investigation, Conceptualization. **Zheni Fei:** Writing – review & editing, Software. **Christopher Vogel:** Writing – review & editing, Writing – original draft, Supervision, Methodology, Investigation, Funding acquisition, Conceptualization.

Declaration of competing interest

The authors declare the following financial interests/personal relationships which may be considered as potential competing interests: Christopher Vogel reports financial support was provided by UK Research and Innovation. If there are other authors, they declare that they have no known competing financial interests or personal relationships that could have appeared to influence the work reported in this paper.

Acknowledgements

The authors thank the reviewers for their helpful comments. The authors acknowledge the support of the UKRI through CRV's Future Leaders Fellowship MR/V02504X/1.

References

[1] Hermann Glauert, Airplane propellers, Aerodyn. Theory (1935).
[2] Wen Zhong Shen, Robert Mikkelsen, Jens Nørkær Sørensen, Christian Bak, Tip loss corrections for wind turbine computations, Wind. Energy 8 (4) (2005) 457–475.
[3] RHJ Willden, X Chen, SW Harvey, H Edwards, CR Vogel, K Bhavsar, T Allsop, J Gilbert, Hannah Mullings, M Ghobrial, et al., Tidal turbine benchmarking project: Stage I-Steady flow blind predictions, in: 15th European Wave and Tidal Energy Conference, Bilbao, 2023, p. 574.
[4] Jens Nørkær Sørensen, Aerodynamic aspects of wind energy conversion, Annu. Rev. Fluid Mech. 43 (2011) 427–448.
[5] M.L. Buhl Jr., New Empirical Relationship between Thrust Coefficient and Induction Factor for the Turbulent Windmill State, Technical Report NREL/TP-500-36834, 15016819, National Renewable Energy Laboratory, Golden, CO, USA, 2005.
[6] T. Burton, N. Jenkins, D. Sharpe, E.A. Bossanyi, Wind Energy Handbook, second ed., Wiley, Chichester, UK, 2011.
[7] G. Bangga, T. Lutz, E. Jost, E. Krämer, CFD studies on rotational augmentation at the inboard sections of a 10 MW wind turbine rotor, J. Renew. Sustain. Energy 9 (2) (2017) 023304.
[8] Ralph C. Smith, Uncertainty Quantification: Theory, Implementation, and Applications, vol. 12, Siam, 2013.
[9] Dongbin Xiu, Numerical Methods for Stochastic Computations: A Spectral Method Approach, Princeton University Press, 2010.
[10] Jonas Kusch, Martin Frank, Intrusive methods in uncertainty quantification and their connection to kinetic theory, Int. J. Adv. Eng. Sci. Appl. Math. 10 (2018) 54–69.
[11] Serhat Hosder, Robert Walters, Rafael Perez, A non-intrusive polynomial chaos method for uncertainty propagation in CFD simulations, in: 44th AIAA Aerospace Sciences Meeting and Exhibit, 2006, p. 891.
[12] John Schaefer, Serhat Hosder, Thomas West, Christopher Rumsey, Jan-Renee Carlson, William Kleb, Uncertainty quantification of turbulence model closure coefficients for transonic wall-bounded flows, AIAA J. 55 (1) (2017) 195–213.
[13] Bruno Sudret, Global sensitivity analysis using polynomial chaos expansions, Reliab. Eng. Syst. Saf. 93 (7) (2008) 964–979.
[14] H. Christopher Frey, Sumeet R. Patil, Identification and review of sensitivity analysis methods, Risk Anal. 22 (3) (2002) 553–578.
[15] Ilya M. Sobol, Global sensitivity indices for nonlinear mathematical models and their Monte Carlo estimates, Math. Comput. Simulation 55 (1–3) (2001) 271–280.
[16] Yassine Ouakki, Amar Amour, Abdelaziz Arbaoui, Uncertainty analysis of a blade element momentum model using GSA and GLUE methods, in: International Conference on Artificial Intelligence & Industrial Applications, Springer, 2023, pp. 299–311.
[17] Jason Jonkman, Sandy Butterfield, Walter Musial, George Scott, Definition of a 5-MW Reference Wind Turbine for Offshore System Development, Technical Report, National Renewable Energy Lab.(NREL), Golden, CO (United States), 2009.
[18] Christian Bak, Frederik Zahle, Robert Bitsche, Taeseong Kim, Anders Yde, Lars Christian Henriksen, Morten Hartvig Hansen, Jose Pedro Albergaria Amaral Blasques, Mac Gaunaa, Anand Natarajan, The DTU 10-MW reference wind turbine, in: Danish Wind Power Research 2013, 2013.
[19] A. Wimshurst, RHJ Willden, Analysis of a tip correction factor for horizontal axis turbines, Wind. Energy 20 (9) (2017) 1515–1528.
[20] D.D. Apsley, P.K. Stansby, Unsteady thrust on an oscillating wind turbine: comparison of blade-element momentum theory with actuator-line CFD, J. Fluids Struct. 98 (2020) 103141.
[21] S.A. Ning, A simple solution method for the blade element momentum equations with guaranteed convergence, Wind. Energy 17 (9) (2014) 1327–1345.
[22] Géraud Blatman, Bruno Sudret, Adaptive sparse polynomial chaos expansion based on least angle regression, J. Comput. Phys. 230 (6) (2011) 2345–2367.
[23] The QBlade software, 2023, https://qblade.org/downloads/. (Accessed 12 December 2023).
[24] David Marten, QBlade: a modern tool for the aeroelastic simulation of wind turbines, 2020.
[25] Nestor V Queipo, Raphael T Haftka, Wei Shyy, Tushar Goel, Rajkumar Vaidyanathan, P Kevin Tucker, Surrogate-based analysis and optimization, Prog. Aerosp. Sci. 41 (1) (2005) 1–28.

[26] Michaël Baudin, Anne Dutfoy, Bertrand Iooss, Anne-Laure Popelin, OpenTURNS: An industrial software for uncertainty quantification in simulation, in: Roger Ghanem, David Higdon, Houman Owhadi (Eds.), Handbook of Uncertainty Quantification, Springer International Publishing, Cham, ISBN: 978-3-319-11259-6, 2016, pp. 1–38, http://dx.doi.org/10.1007/978-3-319-11259-6_64-1.

[27] Jack Kelly, Richard Willden, Christopher Vogel, Parameterising the impact of roughness evolution on wind turbine performance, Wind 2 (2) (2022) 415–428.